World Academy of Science, Engineering and Technology
International Journal of Mechanical and Mechatronics Engineering
Vol:10, No:5, 2016

Investigation of the Cooling and Uniformity Effectiveness in a Sinter Packed Bed

Uzu-Kuei Hsu, Chang-Hsien Tai, Kai-Wun Jin

***Abstract*—**When sinters are filled into the cooler from the sintering machine, and the non-uniform distribution of the sinters leads to uneven cooling. This causes the temperature difference of the sinters leaving the cooler to be so large that it results in the conveyors being deformed by the heat. The present work applies CFD method to investigate the thermo flowfield phenomena in a sinter cooler by the Porous Media Model. Using the obtained experimental data to simulate porosity (E), permeability (κ), inertial coefficient (F), specific heat (Cp) and effective thermal conductivity (keff) of the sinter packed beds. The physical model is a similar geometry whose Darcy numbers (Da) are similar to the sinter cooler. Using the Cooling Index (CI) and Uniformity Index (UI) to analyze the thermo flowfield in the sinter packed bed obtains the cooling performance of the sinter cooler.

***Keywords*—**Porous media, sinter, cooling index, uniformity index, CFD.

I. Introduction

WHEN the sinter leaves the sinter cooler and is carried by the conveyor belt, the temperature should be lower than 250 ˚C. Poor cooling effectiveness results in over high or uneven temperatures, which cause deformation and damage the conveyor. Pan et al. [1] reported that yield rates of the sinter products have significant differences with the changes in seasons, where using variable air volume cooling as the cooling process was more favorable in raising the yield for sinter products. Zhao et al. [2] distributed materials with a method by using a roller feeder and a reflecting plate with the sintering machine, where the silo feeds at a fixed point. As the material surface appeared with a "taper stacked" shape, the edges of the sinter were exposed to enforce cooling. Chang et al. [3] designed an air-flow feeding device by combining the principles of fluid mechanics with the sintering site, and studied the parameters that affected particles segregation, such as airflow speed and feed moisture content. Test results showed that yield was best when the airflow speed was 50 m/s. From the above literature review, it can be seen that the sinter cooler cart, stacked with sinters, may be considered as a porous packed bed, while the blower of the sinter cooler enforces convection cooling. The cooling mechanism is strongly affected by the properties of the inside airflow streams of the sinter packed bed. Therefore, it is important to understand resistance properties of the porous packed bed in order to improve the cooling performance of the sinter cooler. This is especially important when conducting the heat transfer analysis with the porous vessel, as the porosity (E), permeability (κ) and inertial coefficient (F) must first be confirmed. The resistance properties of these three have a great influence on the flow.

Vafai et al. [4] considered the boundary and inertia effects of the solid, and used a local average volume approach to derive the transport equations for the flow and heat transfer in porous media. It was found that the solid boundary effects and non-Darcy effects had a significant effect on a flow field with a higher porosity, Prandtl number, and pressure gradient. Benenati et al. [5] discovered the variable changing of the porosity of the inner walls. Chou et al. [6] studied the channeling effect, caused by changes in porosity, towards the flow field and temperature distribution inside the porous media channels. Jones et al. [7] conducted the packed bed experimental research with sphere particles, and indicated that for high Reynolds numbers the boundary layer wall effects must be considered. If the channel to spherical size ratio is too small, the measurement of the packed bed fluid resistance is affected, and therefore an empirical equation within range Re=103–105 was proposed. Vafai [8] analyzed the effects of the changing porosity and inertia forces toward the heat transfer and flow field of the porous medium, to understand the channeling effect caused by changes with the porosity. Hunt et al. [9] conducted experiments by using a fibrous shaped porous medium to explore the thermal dissipation effect at the enforced convection inlet. From theory and experimental results, it was found that a positive correlation existed between the square root of the permeability and product of the fluid velocity. Vafai et al. [10] analyzed the enforced convection for a sphere packed bed, and had found that when numerical research neglects the solid boundary and channeling effects, the experimental and numerical studies would cause error. Shonnard et al. [11] assumed local heat equilibrium to conduct experiments, used point contact to define effective thermal conductivity with the porous medium, and verified with experimental results in initial literature. Tavman [12] analyzed a porous medium formed from the stacking of particles, and compared the difference between the effective thermal conductivity model and experimental results. Tavman then proposed that a single effective thermal conductivity model was unable to apply to every case, as the different porosity and different solid to fluid effective thermal conductivity ratios would both affect the calculation of the effective thermal conductivity.

Andrade et al. [13] studied the classical Darcy's law, and applied numerical simulation to a two-dimensional porous medium with the irregular holes distribution, and used the

U. K. Hsu is with the Department of Aircraft Engineering, Air Force Institute of Technology, Gang-Shen Dis., Kaohsiung City 82063, Taiwan (e-mail: ukhsu@ms48.hinet.net).

C. H. Tai and K. V. Jin are with the Department of Vehicle Engineering, National Pingtung University of Science &Technology, Pin-Tung 912, Taiwan (e-mail: chtai@mail.npust.edu.tw).

Forchheimer equation to modify the correlation equations at different porosity and flow fields. Also via experiments, it was found that as the Reynolds number was higher, the inertia effect increased, and transformed from linear to non-linear. Amiri et al. [14] used the numerical simulation method to study enforced convection within a sphere packed bed, and respectively considered the liquid and solid energy equations, heat dissipation effect, changing porosities, inertia effect and the solid boundary effect. Anything missing among the above assumptions led to errors with research results. Sozen et al. [15] analyzed the condensation of steam of transient enforced convection within a sphere packed bed. Calis et al. [16] used numerical methods to discuss the pressure drop formed in a three-dimensional packed bed channel, and compared with experiments; the average error between the two was only 10%. The numerical simulations and Laser-Doppler Anemometry (LDA) were compared at different Reynolds numbers, where the average error for the friction factor was 20% when comparing the particle size in different channels. Fu et al. [17] used a numerical method to discuss the effect of two-dimensional channel enforced convection on the heat transfer of random porosity porous media. When the average porosity was greater than 0.5, the average Nusselt number significantly increased, and was better than solids which were impenetrable. Therefore, a higher average porosity coordinated with the suitable copper particle size could allow a porous medium with random porosities to have a better heat dissipation effect. Also, with a random porosity distribution, the speed within the porous medium was distributed irregularly, where the channeling effect close to the wall was insignificant.

From the above literature, it can be seen that in order to understand the heat transfer behavior of a flowing fluid within a porous medium, an experimental approach is necessary. Also, different porous media (such as sand packed bed, spherical copper particles packed bed, aluminum foam material, etc.) would have different influences on the material properties of itself, exterior shape or packing method with the characteristics of the formed porosity and heat transfer. Therefore, this study shall first use experimental methods to obtain the pressure drop and heat transfer characteristics, and use a numerical simulation approach to explore the behavior of the sinter cooler towards the cooling heat dissipation. By mechanisms of the thermal flow field, measures for improving the cooling performance of the sinter cooler are proposed.

II. Study Materials

A. Physical Problem

A typical sinter cooler slowly rotates counterclockwise, with one complete rotation taking approximately 40 minutes. The mechanism of the cooling is shown in Fig. 1. The airstreams from the two blowing fans enter the air duct beneath the ring-shaped sinter cooler (air passage part/ clear channel). Since the duct walls form a closed space, the pressure drives the air towards the sinter above, where this wind penetrates through the gaps of the sinter and carries away waste heat to reduce the temperature (sinter layer part/ porous media). As the sinter exits the sintering machine and fills the cooler, the larger sizes usually accumulate closer to the inner wall, and the smaller sizes closer to the outer wall [18], [19]. For larger size particles, the porosity of the packed sinter also becomes larger, and the resistance for the air passing through becomes smaller; the situation is opposite for smaller particles. The reason for the sinter cooler's poor efficiency is that the air cannot evenly penetrate to the surface of every sinter, and an even overall cooling performance cannot be obtained. As a result, this causes an overlarge temperature difference on the conveyor as the sintered particles drop from the cooler exit. This study discusses how the arrangement methods of the sinter on the sinter cooler affect the uniformity in heat dissipation.

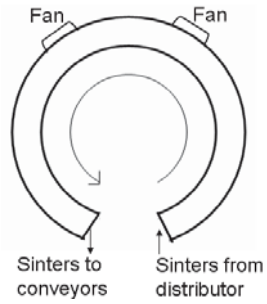

Fig. 1 Illustration of the actuator mechanism of the sinter cooler (Model A)

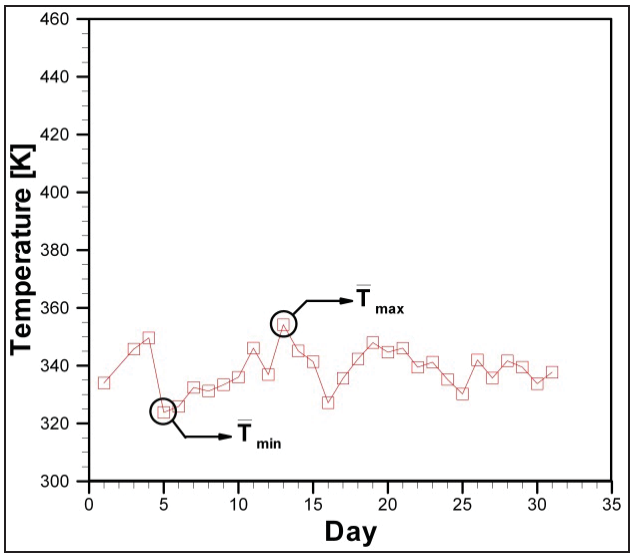

Fig. 2 Monitoring of sinter outlet mean for a 31-day period

B. Improvement Indicators

A temperature recording device was installed at the outlet of a sinter cooler of a typical sintering site. The temperature of the falling sinter onto the conveyor is recorded every six minutes. During a 31-day period, the mean maximum ($\overline{T}_{max}$) and minimum ($\overline{T}_{min}$) temperatures were 50 ℃ and 81℃ (323 *K* and 354 *K*), respectively, as shown in Fig. 2. (There were 240 temperature recordings for each day, the mean temperature value shown in the figure was an average based with 240 temperature recordings.)

When a numerical simulation approach is used to discuss the cooling performance and outlet temperature uniformity of the sinter cooler, indicators are to be defined in order to determine if the changes in the geometric shape of the air channel improved the cooling performance and temperature uniformity. Therefore, specific indicators were used for analysis: the temperature cooling index and uniformity index.

1. Cooling Index

$$CI = \frac{\overline{T}}{\overline{T}_{\exp}} \tag{1}$$

where *CI* is the temperature cooling index, $\overline{T}$ is the mean numerical simulation temperature at the sinter outlet, and $\overline{T}_{\exp}$ is the actual mean temperature at the sinter outlet (339 *K*) that is measured based on 31 days. When the cooling index is less than 1, the cooling performance is better.

2. Uniformity Index

$$UI = \frac{\sum_{i=1}^{n}\left|T_i - \overline{T}\right|}{n} \cdot \frac{1}{\Delta T_{\exp}} \tag{2}$$

where *UI* is the uniformity index, T_i is the sinter temperature at the various points at the outlet, $\overline{T}$ is the numerical simulation mean temperature for the sinter outlet, and ΔT is the difference between the actually measured maximum and the minimum mean temperature for the sinter outlet, where the value was 31 *K*. Therefore, the ratio of the temperature difference with the actual temperature difference at each sinter point can indicate the uniformity of the sinter outlet temperature. When the uniformity index equals 1 it indicates that the temperature difference between the sinter and outlet mean temperature is 31 *K*; i.e., the sinter outlet temperature is rather non-uniform; on the contrary, when the cooling index equals 0, each sinter temperature equals the outlet mean temperature, and thus the sinter outlet temperature is rather more uniform.

From the previous description, the temperature difference at the sinter outlet and mean temperature are therefore the main goal for discussion. In addition, the study for improving the sinter outlet and mean temperature was done by further analysis on changing the sinter arrangement method, or changing the geometric exterior of the air channel, where the final goal is to protect the lifetime usage of the conveyor.

C. Numerical Methods

The study was to discuss the cooling performance of the cooler applied to the sinter. The computational fluid dynamics (CFD) approach was used to solve the speed, pressure and temperature field according to steady state three-dimensional governing equations. By applying the finite volume method SIMPLE algorithm [20], and combined with multiple moving reference frames, standard turbulent model [21] and the Brinkman- Forchheimer-Darcy porous media model [22]-[24], the flow field and temperature field of the sinter on the sinter cooler were solved.

1. Governing Equations

The study uses the CFD method to solve the three-dimensional Navier-Stokes equations at steady-state.

i. Continuous Equation

$$\nabla \cdot \vec{v} = 0 \tag{3}$$

ii. Momentum Equation

(a) Air channel

$$\nabla \cdot \left(\vec{v}_r \vec{v}\right) + \left(\vec{\omega} \times \vec{v}\right) = -\nabla \cdot \left(\frac{p}{\rho}\right) + \nabla \cdot \left(\frac{\vec{\tau}}{\rho}\right) \tag{4}$$

(b) Sinter area

$$\nabla \cdot \left(\vec{v}_r \vec{v}\right) + \left(\vec{\omega} \times \vec{v}\right) = -\nabla \cdot \left(\frac{p}{\rho}\right) + \nabla \cdot \left(\frac{\vec{\tau}}{\rho}\right) + \frac{S_i}{\rho} \tag{5}$$

iii. Energy Equation

(a) Air channels

$$\nabla \cdot \left(\vec{v}_r E + p\vec{u}_r\right) = \frac{k_f}{\rho}\nabla^2 T \tag{6}$$

(b) Sinter area

$$\nabla \cdot \left(\vec{v}_r E + p\vec{u}_r\right) = \frac{k_{eff}}{\rho}\nabla^2 T + \frac{S_q}{\rho} \tag{7}$$

where $\vec{u}_r = \vec{\omega} \times \vec{r}$ is the relative velocity, $\vec{u}_r$ is the rotation speed, $\vec{\omega} \times \vec{v}$ includes the Coriolis acceleration and centripetal acceleration, S_i is the fluid which flows through the porous medium and creates pressure loss, E is the total energy, and k_{eff} is the effective thermal conductivity. For the equation $S_q = \dot{m}\left(T_i - T_o\right)$, S_q is the heat transfer amount of the sinter, T_i is the sinter inlet temperature when entering the cooler, and T_o is the sinter outlet temperature when leaving the cooler. In the equation $\dot{m} = (1-\gamma)\rho_s C_s \vec{u}_r A$, $\dot{m}$ is the heat emission rate, γ is the porosity, ρ_s is the sinter density, C_s is the sinter specific heat, and A is the cross section area.

2. Turbulent Model

The Reynolds stress tensor is defined by $-\rho\overline{u_i' u_j'}$, which can be redefined by the Boussinesq's assumption as:

$$-\rho\overline{u_i' u_j'} = \mu_t\left(\frac{\partial u_i}{\partial x_j} + \frac{\partial u_j}{\partial x_i}\right) - \frac{2}{3}\rho \mathrm{k}\delta_{ij} \tag{8}$$

$$\mu_t = C_\mu \rho \frac{\kappa^2}{\varepsilon} \tag{9}$$

where μ_t is the turbulent viscosity, k is the turbulent kinematic energy, and δ_{ij} is the unit vector.

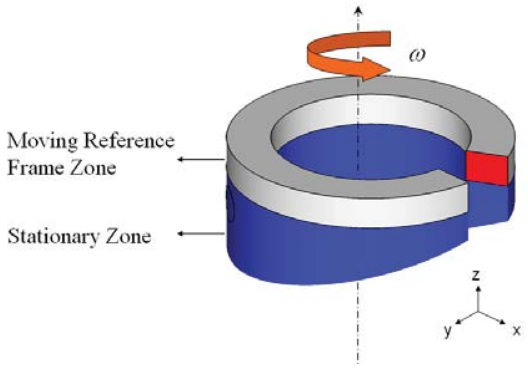

Fig. 3 Rotating reference frame system illustration (Model A)

This study used the standard *k-ε* turbulent model [21], where the transport equation for the turbulent kinematic energy, *k*, and turbulent kinetic energy dissipation rate, *ε*, is:

$$\frac{\partial}{\partial x_i}\left(k\overline{u_i}\right)=\frac{1}{\rho}\frac{\partial}{\partial x_i}\left[\left(\mu+\frac{\mu_t}{\sigma_k}\right)\frac{\partial k}{\partial x_i}\right]+\frac{G_k}{\rho}-\varepsilon \tag{10}$$

$$\frac{\partial}{\partial x_i}\left(\varepsilon\overline{u_i}\right)=\frac{1}{\rho}\frac{\partial}{\partial x_i}\left[\left(\mu+\frac{\mu_t}{\sigma_\varepsilon}\right)\frac{\partial \varepsilon}{\partial x_i}\right]+\frac{C_{1\varepsilon}}{\rho}\frac{\varepsilon}{k}\left(G_k\right)-C_{2\varepsilon}\frac{\varepsilon^2}{k} \tag{11}$$

The terms in (10) and (11) are defined as follows:

$$G_k=\mu_t S_s^2 \tag{12}$$

$$S_s=\sqrt{2S_{ij}S_{ij}} \tag{13}$$

$$S_{ij}=\frac{1}{2}\left(\frac{\partial\overline{u_i}}{\partial x_j}+\frac{\partial\overline{u_j}}{\partial x_i}\right) \tag{14}$$

In the above equations, the coefficients C_1=1.44, C_2=1.92, σ_κ=1.0, σ_ε =1.3, and C_μ=0.099 are all empirical constants created in the turbulent kinetic energy of *G*.

3. Multiple Rotating Reference System

As shown in Fig. 3, the overall sinter cooler can be divided into two parts: the bottom layer is the airflow route, and the top layer is the sinter area. This paper discusses the effect of the steady state flow field on the temperature by changing the exterior of the sinter cooler air channel. However, since the actual situation of the cooling was performed by the sinter area using the cart to enable the sinter area to rotate on the sinter cooler to perform heat dissipation, the air channel overall was a fixed inertia system, and the fluid flows within the channel were at steady state; furthermore, the sinter area rotated counterclockwise in relation to the air channel conduct, and was seen as a rotary system. Since the rotation speed was 0.0025 (rad/s), its interaction influence on the air channel was rather small. If the two flowing areas were assumed to be nearly identical, the multiple rotating reference frame can thus be used to deal with the problems for a non-inertial system. Also, the interface between the fixed and rotating systems was assumed to be flowing at steady state, in which the absolute speeds were the same, and thus followed the mass conservation law for fluids. In addition, a sophisticated mobile computing grid system was not required for additional calculations with the transient interactions among flow changes.

4. Porous Media Model

Since the empirical equation of Darcy's Law [22] applies only to slow-flowing, or for media with very low permeation or porosity, Forchheimer [23] indicated that the surface drag had a very important relation to the form drag and friction caused by the porous medium at large flowing speeds. Therefore, the influence of the inertia term was considered. Furthermore, there are many situations where the porous medium, with limited inside space, contains impermeable walls; and then the friction resistance of the wall needs to be considered. This resistivity can be added to the Darcy's resistance which was caused by the particle itself. Brinkman [24] indicated that the friction force due to the limited inside space and impermeable wall contact was to be considered in order to meet with the wall's non-slip condition. Based on the improvement theories of the above literature, the sinter area in this study used a porous media model for simulation, and obeyed the Brinkman-Forchheimer-Darcy equation. The equation is defined as

$$S_i=\frac{\partial p}{\partial x_i}=-\frac{\mu}{K}u_i-\frac{F\rho}{\sqrt{K}}u_i^2 \tag{15}$$

where μ is the viscosity coefficient and ρ is the density. The other two parameters, the permeability, K, and inertial coefficient, F, were determined by the wind tunnel experiments.

D. Sinter Experiments with the Pressure Drop and Heat Transfer Characteristics

Literature review has demonstrated that the flowing characteristics within the porous medium vessel strongly affect heat transfer characteristics. Therefore, to understand the heat transfer characteristics of the flow of the sinter packed bed, it is necessary to first understand the flow resistance properties; especially when heat flux calculation analysis is conducted for the sinter packed bed flow, the sinter packed bed porosity (E), permeability (κ) and inertial coefficient (F) are the necessary input parameters. These three resistance characteristics of the porous medium are greatly related with the flow effect. The permeability (κ) and inertial coefficient (F) of the porous medium are related with the inside structure composition and porosity (E). The more acceptable permeability (κ) and inertial coefficient (F) equation at the present is referred to a dense, sphere packed bed. The irregular shapes of the sinter are not suitable for any known empirical equation. This study used experiments to measure the materials properties such as the sinter density (ρ), equivalent effective thermal conductivity (k_{eff}), and specific heat (C) to understand the heat transfer characteristics. Also, by experimental methods, the permeability (κ) and inertial coefficient (F) of the sinter packed

bed was determined, and the flow resistance within the channels was discussed to serve as the fundamental study for numerical simulation with the heat transfer characteristics.

1. Sinter Experiments with the Pressure Drop Characteristics

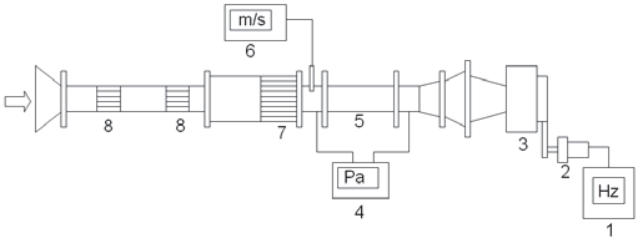

1. Inverter
2. Motor
3. Blower
4. Pressure gauge
5. Test section
6. Anemometer
7. aluminum foams
8. Honey-comb

Fig. 4 Wind tunnel equipment

i. Equipment

The experiment constructed an experimental wind tunnel platform to measure the fluid pressure drop characteristics of the sinter packed bed. The equipment is as shown in Fig. 4, and is mainly divided into four sub-systems:

Air source supply system: The working fluid in the experiment was air, and a blower served as the air source device. A digital frequency converter controlled the rotational speed of the blower's motor to regulate the airflow amount. The AC frequency range of the frequency converter was controlled at 15 Hz–60 Hz. Under the control of the same frequency changes, the airflow amount would form different wind speeds based on the different particle sizes.

Wind tunnel: Opened and suction type. After air enters the contractible bell nozzle, it then passes through a rectifying section of a honeycomb structure and porous aluminum material so that the airflow has a uniform flow speed before it enters the test section, and then the flow finally enters the test section.

Test section: The rectangular channel was made from electric wood material with a 10 mm thickness. The length, weight, and height of the test section were 360 mm × 85 mm × 85 mm. The packed sinter was placed in this area, and the front and back cross sections were fixed with iron gauze wire, respectively. The distribution of the sinter packed bed is as shown in Fig. 5 (upper lid opened). The experiments were conducted with two different sinter packed beds with the equivalent particle sizes of 1 mm and 5 mm. The bottom center of the test section was installed with a number of pressure holes along the flow direction. The pressure holes were connected to a switch valve through pipelines, and then connected to a differential pressure gauge to measure the changes in pressure.

Data collection system: The wind meter was placed at the front end of the test section to measure the average airflow velocity within the wind tunnel, and static pressure measuring holes were arranged at different positions within the test section, where the differential pressure gauge was used to monitor and record the pressure changes at each point.

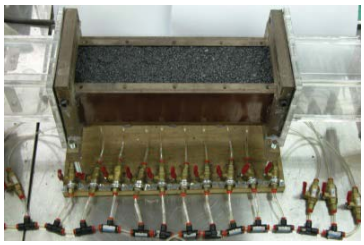

(a) $d_p = 0.1\ cm$

(b) $d_p = 0.5\ cm$

Fig. 5 Test section of the wind tunnel

ii. Measurement Procedure

After each measuring instrument was calibrated, the pipelines in the experiment were tested for any leakage to ensure the correctness with the pressure measurement. Experiments for the sinter pressure drop characteristics were conducted with the two different particle size groups, respectively. The work fluid used air at normal temperature, where the pressure drop was measured as the air flowed through the sinter to obtain the sinter permeability (κ) and inertial coefficient (F).

iii. Similarity Analysis of the Sinter Cooler within the Test Section

Due to the limitations of the wind tunnel size, if the original size of sinters on the sinter cooler were directly placed into the wind tunnel test section, the channeling effect at the wall would greatly affect the accuracy of the experiments. At the same time, the similarities for the multiple holes were unable to be compared by analogy for the actual sinter cooler. Therefore, the sizes of the sinter particles were required to adjust to the width of the sinter cooler and the width of the wind tunnel test section for the experiment. The size was similarly shrunk based on the Darcy number (Da), where the original equivalent particle sizes (Dmin ~ Dmax) of the sinters on the sinter cooler were 0.05–0.2 m. In this study, the sinter cooler width (De) was 3.4 m, the wind tunnel test section width (dexp) was 0.085 m, and the Darcy number (Da) similarity was calculated as below:

$$\frac{D_{\max}}{D_e} = \frac{0.2}{3.4} = \frac{d_{\max}}{d_{\exp}} = \frac{d_{\max}}{0.085} \tag{16}$$

$$d_{\max} = 0.005m$$

$$\frac{D_{\min}}{D_e} = \frac{0.05}{3.4} = \frac{d_{\min}}{d_{\exp}} = \frac{d_{\min}}{0.085} \tag{17}$$

$$d_{\min} = 0.00125m$$

The final obtained equivalent particle diameters for the packed sinters within the test section are respectively shown in Table I.

TABLE I
SINTER SIZE CHART

	sinter d_{min}	**sinter d_{max}**
sinter cooler particle size (m)	0.05	0.2
test section particle size (m)	0.00125	0.005
porosity	0.395	0.545

2. Data Processing and Uncertainty Analysis

The measured pressure drop (Dp) and average wind speed (U) in the experiments can be rearranged into dimensionless parameters, the friction coefficient (f), Reynolds number (Re_{H}) and Darcy number (Da). The three dimensionless parameters are defined as:

$$f = \frac{\Delta p}{0.5\rho U^2} \cdot \frac{H}{L} = 2\left(\frac{1}{\mathrm{Re}_H \cdot Da} + \frac{F}{\sqrt{Da}}\right) \tag{18}$$

$$\mathrm{Re}_H = \frac{\rho UH}{\mu} \tag{19}$$

$$Da = \frac{K}{H^2} \tag{20}$$

where Dp is the test section inlet and outlet between pressure drop, L is the test section channels length, H is the test section channels height, U is the fluid average velocity, K is the permeability, and F is the inertial coefficient.

The overall experimental errors include measurement and calculation errors, where the uncertainty with measurements was caused by the errors of the instrument system itself, and man-made reading errors. Calculation errors were formed as the measured values were calculated. The uncertainty analysis in this experiment applied the methods by Kline et al. [25] and Moffat [26]. The experimental results were measured through the series of experiments, and thus the experimental results R is the function of experimental measured parameters (x1, x2, x3, ……, xn). When xi creates a change amount, xi, R shall also create a change amount, Ri. Thus the uncertainty (uR) caused by xi can be summarized with the following equations:

$$R = R\left(x_1, x_2, x_3, ..., x_n\right) \tag{21}$$

$$\delta R_i = \frac{\delta R}{\delta x_i}\delta x_i \tag{22}$$

$$\frac{\delta R_i}{R} = \frac{1}{R} \cdot \frac{\partial R}{\partial x_i} \cdot \delta x_i = \frac{x_i}{R} \cdot \frac{\partial R}{\partial x_i} \cdot \frac{\delta x_i}{x_i} \tag{23}$$

$$u_R = \frac{x_i}{R} \cdot \frac{\partial R}{\partial x_i} \cdot u_{xi} \tag{24}$$

If u_R is expressed as the experimental result uncertainty function, (u_1, u_2, u_3, ……, u_n) is then the uncertainty for each measured experimental measure parameter. The uncertainty equation for the experimental results and measured experimental parameters is as below:

$$u_R = \pm\left[\left(\frac{x_1}{R} \cdot \frac{\partial R}{\partial x_1} \cdot u_1\right)^2 + \left(\frac{x_2}{R} \cdot \frac{\partial R}{\partial x_2} \cdot u_2\right)^2 + \left(\frac{x_3}{R} \cdot \frac{\partial R}{\partial x_3} \cdot u_3\right)^2 + ... + \left(\frac{x_n}{R} \frac{\partial R}{\partial x_n} \cdot u_n\right)^2\right]^{\frac{1}{2}} \tag{25}$$

Such related parameters are the pressure drop (Dp), average flow speed (U), permeability (κ), inertial coefficient (F), equivalent effective thermal conductivity (k_{eff}), specific heat (C), density (ρ), non-dimensional parameters friction coefficients (f), Reynolds number (Re_{H}) and Darcy number (Da), where the uncertainty Figs. 5 (a) and (b) were ±2.0%, ±2.0%, ±4.2%, 4.6%, ±3.6%, ±3%, ±2.87%, ±3.9%, ±3.1% and ±4.4%, respectively.

III. Computational Model and Boundary Conditions

A. Computational Model

The ranges of the rotation angle, overall height and inner and outer diameter for the sinter cooler were -20° ≤ θ≤ 313°, -2.7 ≤ z/H ≤ 1.0 and 2.8 ≤ r/H ≤ 4.0, respectively. The air channel was located at the bottom layer of the sinter cooler (-20° ≤θ ≤ 313°, -2.7 ≤ z/H ≤ 0.0, 2.8 ≤ r/H ≤ 4.0), and installed with two blowing fans for the cooling mechanism, as shown in Fig. 6. The working performances of the blowing fans are given in Table II. Before performing with numerical simulation calculations, a grid system was to be established based on the geometric shape of the simulation. In this study, the grid allocations in all grid system calculations were based on a structuralized grid system. This study respectively changed the sinter arrangement methods, and changed the geometric exterior channel to discuss and analyze the sinter cooler.

TABLE II
PERFORMANCE CHART OF THE SINTER COOLER BLOWING FAN

Air volume (m^3/min)	12,780
Pressure (mm WC)	240
Cooler fan motor	420×2

B. Boundary Conditions

This study simulated the introduction of gas by a blowing fan into the air channel under the sinter cooler. The sinter above the cooler carries high temperatures due to the sintering process, and then moves along with the cooler as the cooler rotates. Furthermore, the cooling gas within the air channel flows upwards toward the sinter area to dissipate heat. In this study, the boundaries were defined, which included the inlet

boundary, outlet boundary, wall boundary and porous media area. The flow field was expressed by mathematical methods, and the physical flux as it passed through each boundary was calculated. The calculation was then applied to the governing equations.

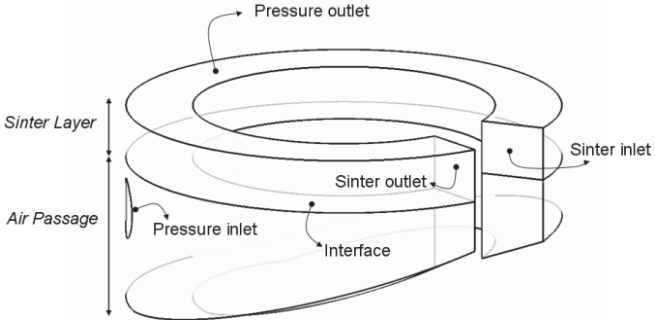

(a) Isometric view (Model A)

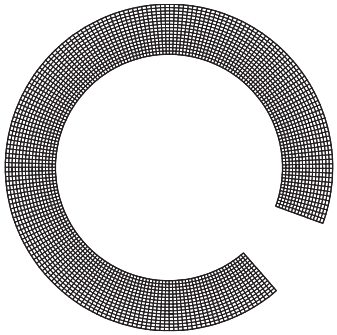

(b) Top view

Fig. 6 Geometry of the site cooler and its air passage

1. Inlet Boundary Condition

Air was selected as the gas fluid, where the inlet pressure was fixed at 2352 Pa, and temperature at 300 K. The sinter inlet mean temperature was 700 K. According to the description for the sinter entering the sinter cooler, the temperature of the sinter itself varies according to the difference in particle size. At the inner side of the cooler, the temperature of the large particles was 900 K, whereas at the outer side the temperature of the small particles was 500 K. In addition, the temperature distribution was assumed to change linearly. The time to deliver the sinter from inside to outside by the cart was 40 minutes, thus the cart rotation speed was defined to be 0.0025 rad/s.

2. Outlet Boundary Condition

The outlet air flow was simulated to flow through the porous medium to the outside atmosphere. Therefore, the outlet boundary condition used standard atmosphere pressure.

3. Wall Boundary Condition

Not only does the fluid satisfy the impermeable condition as it passes the walls, but it also satisfies the no-slip condition. Thus the surrounding wall of the sinter cooler constituted an adiabatic, no-slip wall.

4. Sinter Area

The area obeys the Brinkman- Forchheimer-Darcy flow model. Furthermore, the measured pressure drop and heat transfer characteristics of the sinister material are substituted into the model to define the sinter material's parameters.

TABLE III
INDIVIDUAL CASES WITH THE SINTER ARRANGEMENT

Model	Characteristics
A_1	Sinter porosity is larger at the inner position, and linearly decreases as the radius is increased
A_2	Large sinter porosity at the radius center, and linearly decreasing towards the two ends.
A_3	Porosity linearly decreases with the increasing of height.

TABLE IV
INDIVIDUAL CASE WITH SINTER COOLER BLOCKAGE PLATE LAYOUT

Model	Characteristic	Model	Characteristic
B_1 (A_1)	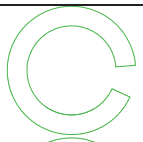	B_4	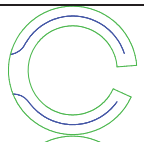
B_2	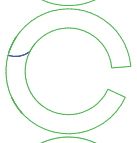	B_5	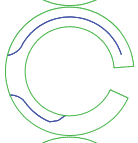
B_3	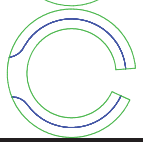	B_6	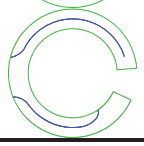

C. Matrix in the Research

1. Individual Cases with Different Sinister Arrangement Changes

This study used three types of arrangement methods on the sinter cooler to discuss which method had the better cooling performance. A polarization analysis device for improvement was then used as reference. The arrangement methods are listed in Table III. A typical arrangement method is shown in Model A1 where the horizontal distribution are the large sinter particles positioned at the outside end, and becoming smaller at the other end; A2 is a horizontal distribution of large sinter particles and porosities located at the middle, and becoming smaller toward both sides; A3 is a vertical distribution with large sinter particles and porosities at the bottom and becoming smaller at the top. The diameters of the sinter particles were all between 5–20 cm. The porosity ranged between 0.4–0.55. Since Model A1 was based on the arrangement of sinter site, it is a typical example for comparison.

2. Individual Cases by Changing the Geometric Exterior of the Sinter Cooler Air Channel

For sinter arrangements under the same method, the method of fluid mechanics was used in this study (sinter particles at the inward position in the radial direction are relatively larger), and discussed the influence with the cooling performance with the geometric changes of the air channel. Three shapes were respectively used, i.e., using a blockage plate, air channel slope,

and groove as the different layouts as to provide improvement for the sinter cooler channel. Individual cases for the blockage plate B1–B6: The layout methods for the blockage plate are given in Table IV. Individual cases for the air channel slope C1–C5: The layout methods for the changes in the slope angle change are given in Table V. Individual cases for the sinter cooler air channel groove D1–D3: The layout methods for the changes in the grooves are given in Table V. Individual cases for the changes with the blowing fan inlet temperature E1–E6: The different types of blowing fan inlet temperature changes are given in Table VI.

TABLE V
INDIVIDUAL CASE WITH CHANGES OF THE AIR CHANNEL SLOPE GROOVE

Model	Characteristic	Model	Characteristic
C_1		D_1 (A_1)	
C_2		D_2	
C_3		D_3	
C_4			
C_5			

TABLE VI
INDIVIDUAL CASE OF BLOWING FAN INLET TEMPERATURE CHANGE

Model	E_1	E_2	E_3	E_4	E_5	E_6
inlet temperature blowing fan A	300	290	280	273	273	300
inlet temperature blowing fan B	300	290	280	273	300	273

IV. Results and Discussion

A. Scheme Verification

The grid test was conducted by using a two-dimensional flow field, and was used to verify the sinter pressure drop characteristics for the results of the wind tunnel experiments, and to compare the pressure drop changes at different flow speeds. Moreover, the similarities of the two-dimensional flow field are to be further used with the grid size of a three-dimensional flow fields.

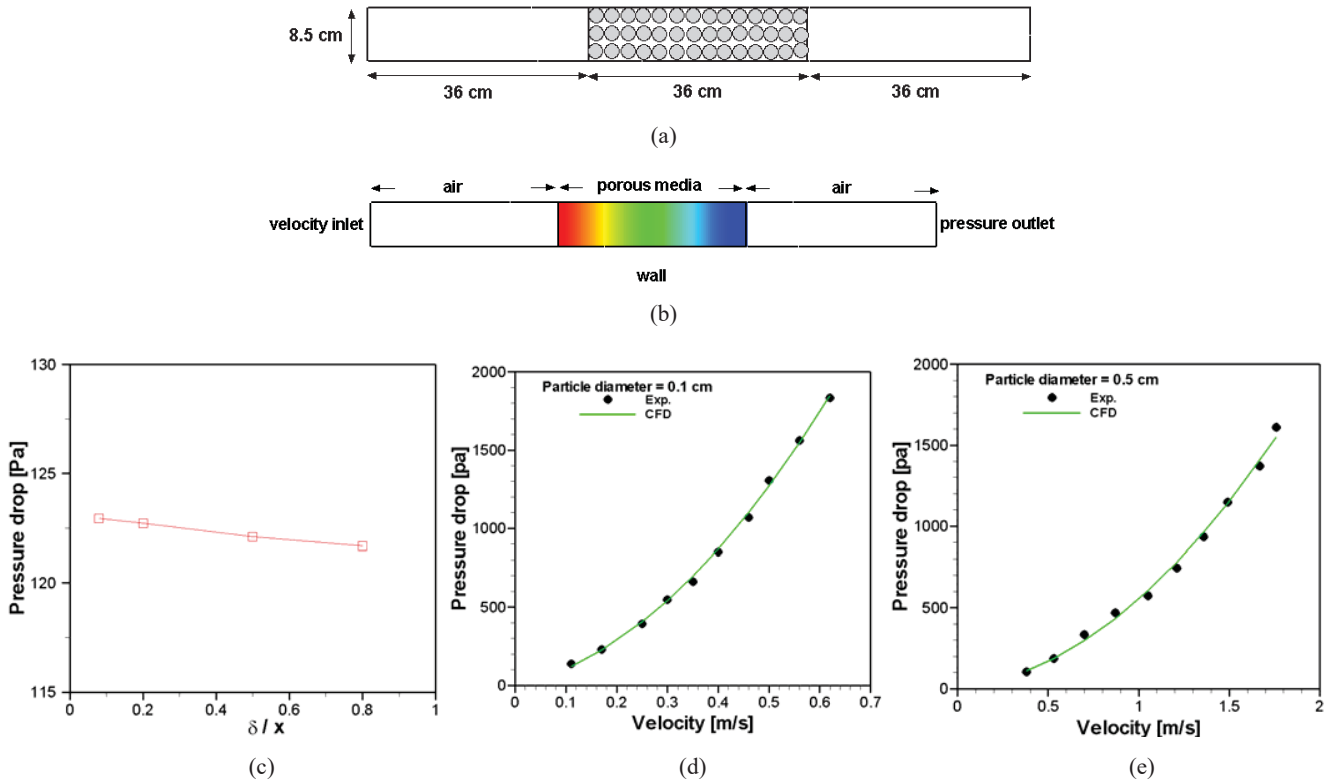

Fig. 7 Experiments and numerical scheme verification for the pressure drop and velocity

The dimensions of the test area for the wind tunnel/sinter pressure drop characteristic experiments were 8.5×8.5×36 cm (W×H×L), as shown in Fig. 7 (a). The geometric structural size for numerical simulation is shown in Fig. 7 (b). In order to save calculation time and reduce the consumption of calculation resources, analysis of the grid is first required, as shown in Fig. 7 (c). Four types of grid systems were respectively established, from dense to sparse grid sizes, δ/x (unit length for the grid distance of the first layer) were 0.08, 0.2, 0.5 and 0.8. From the calculating results of the four types of grid systems, it could be found that under a wind speed of 0.1 m/s or less, the pressure difference trend was almost the same at δ/x= 0.2 and 0.08. However, as the saving of computer calculating resources was considered, the numerical calculation at grid size δ/x=0.2 was

better. The numerical simulation and experiments results were then respectively used to verify the pressure loss relation of sinter particle sizes at 0.1 and 0.5 cm at different wind speeds, where the results are shown in Figs. 7 (d) and (e). It is seen that the simulation results and experiments data appeared with good consistency. The grid similarities were then applied to the grid configuration of a three-dimensional flow field.

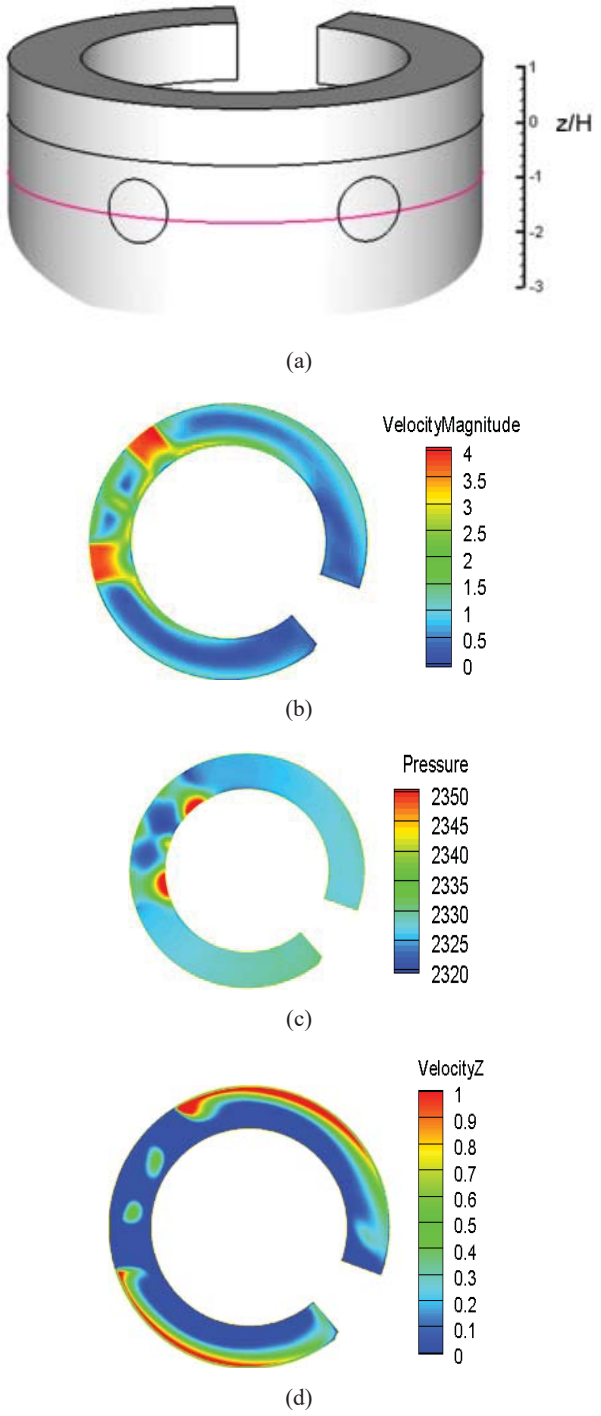

Fig. 8 Speed, pressure and vertical velocity distributions for Model A1 at z/H=-1

B. Effect of Different Sinter Arrangement Methods on the Thermo Flow Field

1. Air Channel Flow Field

Because the maximum wind amount created by the blowing fan was located at the cross section z/H=-1 (as shown in Fig. 8 (a)), the following shall discuss the relation of the pressure, speed and vertical direction speed at z/H=-1. From Fig. 8 (b), it can be seen that the blowing fan blows cooling air at a temperature of 300 K into the air channel. At first, the cooling air collides with the inner wall, and the air flows along the inner wall to the surroundings. Also, the collision of pressure interaction of the two blowing fans occurs, as shown in Fig. 8 (c). The location at this place causes a possible loss in energy, where the cooling air was unable to effectively flow towards the sinter area. By the speed vector approach, it can be seen that besides the cooling air interaction collisions causing return flow by the two blowing fans, the cooling air additionally started to separate from the inner wall due to the centrifugal force effect and flowed toward the outer wall (as shown in Fig. 8 (d)) and formed a return flow area at the end of the air channel as the airflow collided into the wall. From the cross section z/H= -1 in Fig. 8 (d), the vertical direction speed profile is shown. The cause of the outer vertical direction speed was because after the introduction of cooling air from the blowing fan, the air along the inner wall started to flow outwards. As shown in Fig. 9, the vertical speeds at cross sections a-a', b-b', c-c' and d-d' of the air channel ($-2.7 \leq z/H \leq 0.0$) are expressed in vectors, where a', b', c' and d' are the outer walls. From cross section c-c', it can be significantly seen that the speed vector flowed to the bottom of the air channel, and then flowed outwards with a direction along the outer wall. This was the reason for the formation of the vertical direction speed at the outer wall.

2. Sinter Area Flow Field

Although different sinter arrangement methods were performed at the sinter area, the flow field mechanism within the air channel was nearly the same if the exterior of the air channel had no changes. Therefore, as the fluid flows though the sinter area, different pressure drop characteristics exist in accordance with the different methods of the sinter arrangement. The sinter arrangement method for Model A1 (typical example) was a horizontal distribution of large sinter particles and porosity at the inner radial direction end, and decreased in size and porosity with a linear relation towards the outer end as the radius increased. In Fig. 9, the flow resistance at the sinter area ($0.0 \leq z/H \leq 1.0$) is relatively smaller as the porosity was smaller, which would become larger for the opposite situation. In Fig. 9 (a), it could be clearly seen that the vertical direction speed is higher as the inner porosity is smaller. The arrangement method in Model A2 was a horizontal distribution of large sinter particles and porosities located at the middle and becoming smaller toward both sides. In Fig. 10, the flow resistance at the sinter area ($0.0 \leq z/H \leq 1.0$) is relatively smaller as the porosity was smaller, which would become larger for the opposite situation. Although the

arrangement method was changed, from Fig. 10 (a) it could be clearly seen that at the center location the vertical direction speed is higher as the inner porosity is smaller. Figs. 8 (b)-(e) show that when the cooling air flowed from the air channel towards the sinter area, due to the relation between the viscosity resistance and inertial resistance of the packed sinters, the speed in the vertical direction of the cooling air flowing towards the sinter area was greatly affected. The arrangement method in Model A3 was a vertical distribution with large sinter particles and porosities at the bottom and becoming smaller at the top. Since the porosity gradually decreases with the height, the vertical direction speed becomes nearly uniform as the cooling air passes the sinter area.

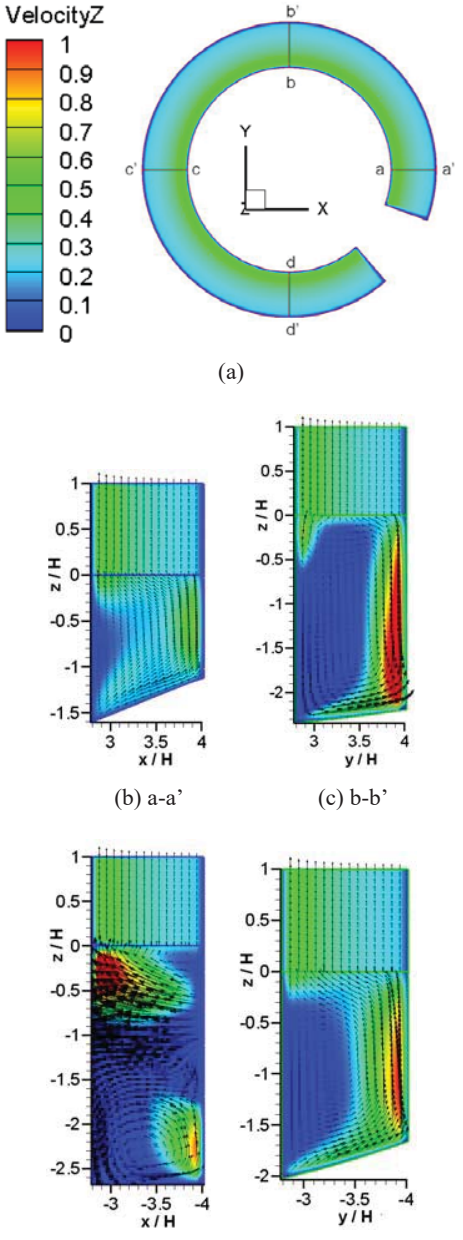

(a) (b) a-a' (c) b-b' (d) c-c' (e) d-d'

Fig. 9 Vertical velocity distribution for Model A1 at various cross sections

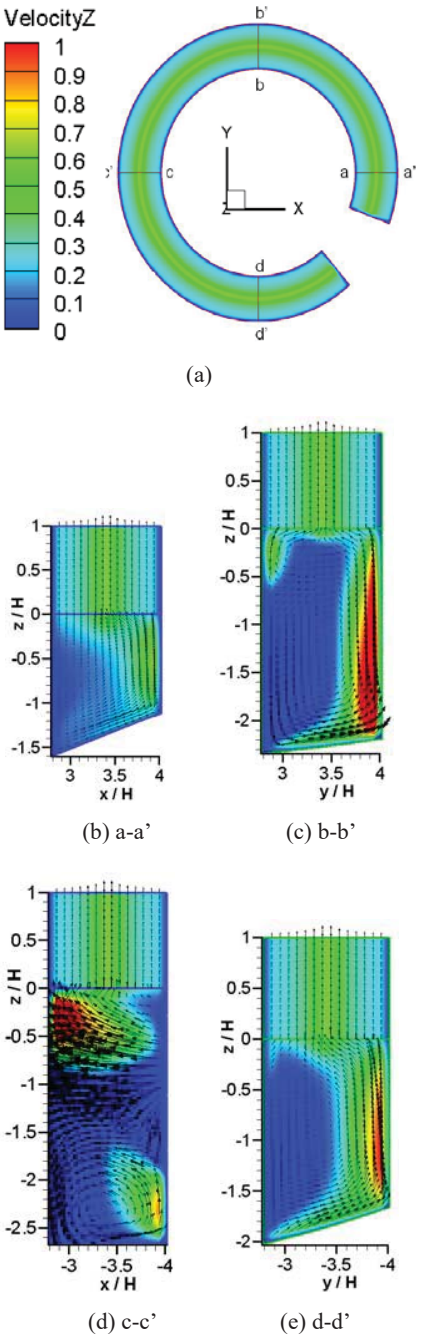

(a) (b) a-a' (c) b-b' (d) c-c' (e) d-d'

Fig. 10 Vertical velocity distribution for Model A2 at various cross sections

TABLE VII
INDIVIDUAL CASE OF SINTER ARRANGEMENT -SINTER OUTLET TEMPERATURE COOLING INDEX (CI) AND UNIFORMITY INDEX (UI)

Model	A_1	A_2	A_3
mean temperature (*K*)	328	326	343
the maximum temperature (*K*)	507	502	584
the minimum temperature (*K*)	300	300	300
temperature difference (*K*)	207	202	284
CI	0.97	0.97	1.01
UI	0.97	0.94	1.39

3. Sinter Area Temperature Field

For locations where the sinter porosity was larger, the cooling air flowed more easily to the location, and thus the heat transfer phenomenon was rather more significant. In Fig. 11, since the sinter arrangement methods were different, although the cross section average velocity in the vertical direction did not had a large difference with the overall change in height, the comparison of the temperature cooling index (CI) and uniformity index (UI) at the sinter outlet (shown in Table VII) showed that the mean outlet temperature of Model A2 was 0.6% less than Model A1 (typical example), whereas with Model A3 the outlet mean temperature was 4.5% higher than Model A1. From the cooling index, the sinter arrangement method by Model A2 was indicated to be better, where the temperature uniformity also dropped 4% lower than Model A1. Therefore, Model A2 (large sinter particles at the center and decreasing toward the two ends in the radial direction) was able to reduce the mean temperature and temperature uniformity at the sinter outlet.

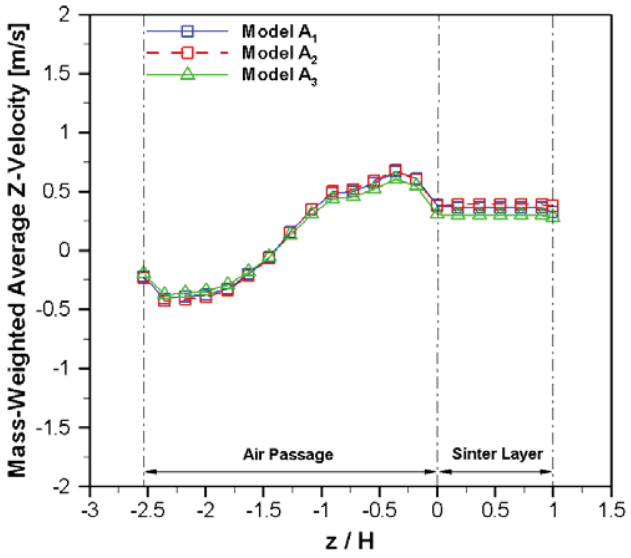

Fig. 11 Models A1–A3, different height cross section vertical average velocity relation

C. Effect of Adding Blockage Plates in the Air Channel on the Thermo Flow Field

1. Air Channel Flow Field

For an air channel without blockage plate installation, the interaction collision of the cooling air due to the two blowing fans causes energy consumption. Therefore, the concept of adding blockage plates was purposed to avoid the interaction effect of the cooling air caused by the two blowing fans. By using Model A1 as an example for reference (named as Model B1), the following five sets of blockage plates installed at different positions, respectively, provided a comparison for the typical example of Model B1, where which set provided an enhancing effect for the cooling performance.

As shown in Fig. 12 (b), Model B2 installed a blockage plate to block the interaction interference of the cooling airflow from the two blowing fans. The flow for one of the blowing fans was directed, whereas the other cooling air from the other blowing fan still flowed towards the location of the blockage plate, and formed a loop flow area. Another loop flow area was also formed when the cooling air flowed to the end wall of the air channel. As the sinter cooler blowing fan blew cooling air forwards, the airflow was divided into two paths as it touched with the cooling channel inner wall; one moved along the inner wall flow and flowed towards the sinter area, whereas the other moved along the inner wall flow and flowed downwards to the bottom wall of the air channel, which then continued to flow towards the outer wall. This point had a significantly larger vertical direction speed formed at the outer wall, and was the main reason for having a larger vertical direction speed. However, due to the fans' blowing effect with the cooling airflow, the airflow at the outer wall was dragged along the inner wall and flowed towards the sinter area.

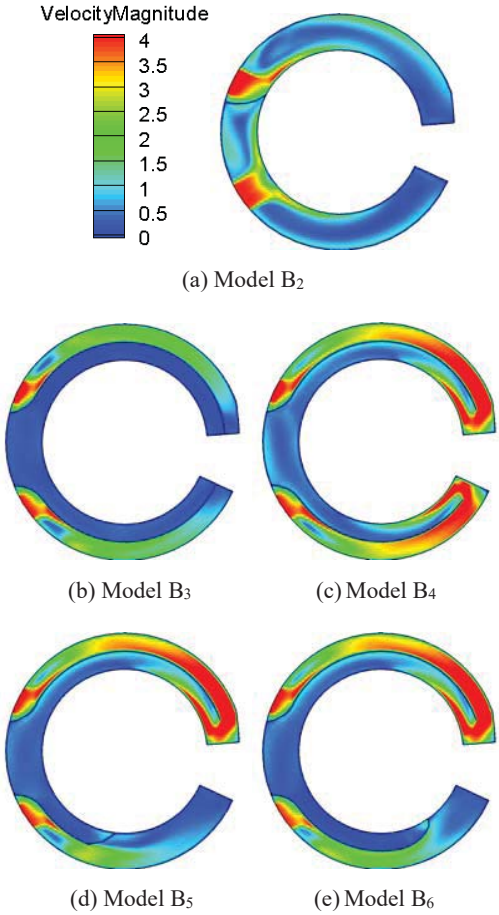

(a) Model B_2

(b) Model B_3 (c) Model B_4

(d) Model B_5 (e) Model B_6

Fig. 12 Models B2–B6, air channel z/H=-1 velocity patterns

The blockage plate layout for Model B3 is as shown in Fig. 12 (c), which allowed the two blowing fans to each have an independent air channel space, where the other air channel space is separated from the blockage plate. In this space, the blown cooling air by the blowing fan is unable to flow through directly, and must flow through the independent air channel, installed with a blowing fan to cross the blockage plate and flow to the location. The cross section in Fig. 13 clearly shows

that the air channel is shortened to half of the channel width due to the adding of the blockage plate, and the cooling air vertical direction speed is concentrated at the outer position.

The blockage plate layout for Model B4 is as shown in Fig. 12 (d), where the blockage plate length is only 0.9 times the length in Model B3. As a result, in this example the air channel was not separated into three independent air channels as in Model B3, but rather formed a connected, looped, air channel. The blown cooling air by the blowing fan was influenced by the opening effect at the end of the air channel due to the blockage plate, and caused the cooling air channel within the inner wall to become longer than in Model B3. The flow speed is raised in the inner channel for the model B4, because the turning airflow from the terminal of the outer channel flows into and influences. Therefore, a local high velocity circulation in occurred near by the top of inner wall as shown in Figs. 13 (e) and (g), and the vertical velocity (Z-direction) is also increased as shown in Fig. 13 (a).

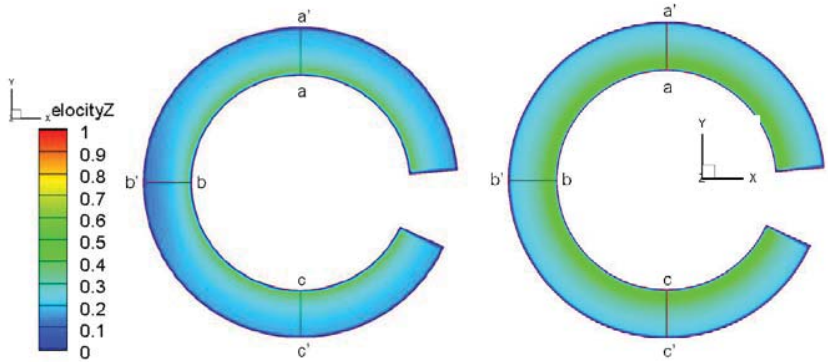

Model B_3 Model B_4

(a) Top view

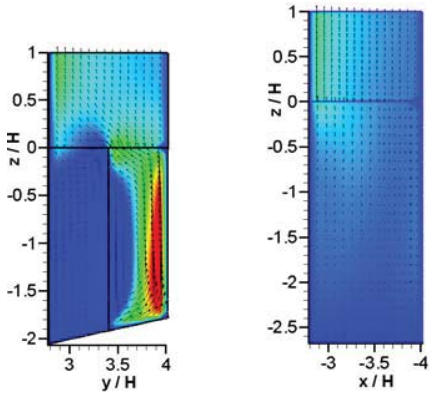

(b) a-a' (Model B_3) (c) b-b' (Model B_3) (d) c-c' (Model B_3)

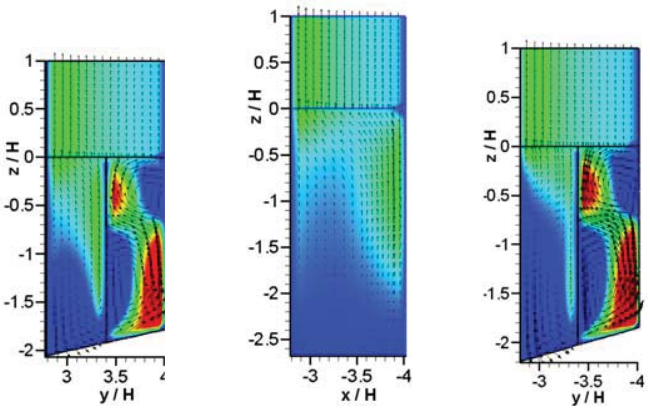

(e) a-a' (Model B_4) (f) b-b' (Model B_4) (g) c-c' (Model B_4)

Fig. 13 Model B_3 and B_4 cross section vertical velocity patterns

For the cooling air which moved along the outer wall and flowed towards the sinter area, due to the airflow effect from the blowing fan, the vertical direction speed area at the outer wall was reduced. This indicated that the cooling air was unable to effectively reach the outer positions of the smaller sinter particles and porosity.

The blockage plate layout for Model B5 is as shown in Fig. 12 (e), where the blockage plate was of an S-shape, and the blowing fan was separated into an independent and gradually widened air channel. Since the air channel gradually increased, the outer wall airflow flowed into the inner wall.

TABLE VIII
INDIVIDUAL CASE OF BLOCKAGE PLATE LAYOUT -SINTER OUTLET TEMPERATURE COOLING INDEX (CI) AND UNIFORMITY INDEX (UI)

Model	B_1	B_2	B_3	B_4	B_5	B_6
Mean temperature (*K*)	328	328	353	328	329	329
Maximum temperature (*K*)	507	507	592	507	507	507
Minimum temperature (*K*)	300	300	300	300	300	300
Temperature difference (*K*)	207	207	292	207	207	207
CI	0.97	0.97	1.04	0.97	0.97	0.97
UI	0.97	0.97	1.35	0.97	0.97	0.97

The blockage plate layout for Model B6 is as shown in Fig. 12 (f), where the blockage plate separated a blowing fan into an independent gradually widening air channel. However, the gradually widening location was rather nearer to the end of the air channel. Similar to the flowing situation in Model B3, since the air channel gradually increased, the outer wall airflow flowed into the inner wall.

2. Sinter Area Flow Field and Temperature Field

Fig. 14 is the vertical direction speed for the sinter outlet surface, where (a) to (f) are respectively of Model B1 to Model B6. Since the sinter arrangement methods all had porosity and particle size linearly decreasing as radius increased, the flow resistance and porosity thus appeared in inverse relation, where the flow speed and porosity formed a proportional relationship. The speed distribution therefore decreased as the radius increased. When compared with Model B1, the differences with the outlet surface speed distribution were: in Model B3 as the inner sinter porosity was larger, the flow resistance was thus relatively smaller, and the cooling air crossed over the blockage plate to flow toward the inner location of the inner sinter area (as shown in Fig. 14 (e)). However, the installation of the blockage plate caused the inner location to become unable to have direct enforced cooling air convection from the blowing fan, and resulted in high temperatures still existing within the insides of the sinter as shown in Fig. 15. As in Fig. 16, where the vertical average velocity changed in relation with the cross section height, the sinter arrangement method was the same but it can be seen in the Fig. 16 that the average velocity in parts of the air channel was smaller than in Model B4, Model B5 or Model B6. This was caused by an inclined angle design with the air channel, where the main expectation was to guide the cooling air towards the sinter area. When the blockage plate was installed so that the air channel was flowing in a winded matter (Fig. 12 (c)), the air moved along the inner location of the air channel slope and flowed downwards, which in turn caused the airflow to be unable to effectively flow through the sinter area. When the cooling performance and temperature uniformity of the sinter outlet surface were compared (Table VIII), it could be realized that the outlet surface mean temperatures of Model B2 and Model B1 were nearly the same, whereas the outlet surface mean temperature in Model B3 was 7.6% higher than Model B1; Model B4 raised 0.1%, Model B5 raised 0.2%, and the blockage plate installation in Model B6 raised the temperature 0.4%. Therefore, the method of adding a blockage plate was unable to obtain a reduction effect for the outlet mean temperature and temperature uniformity.

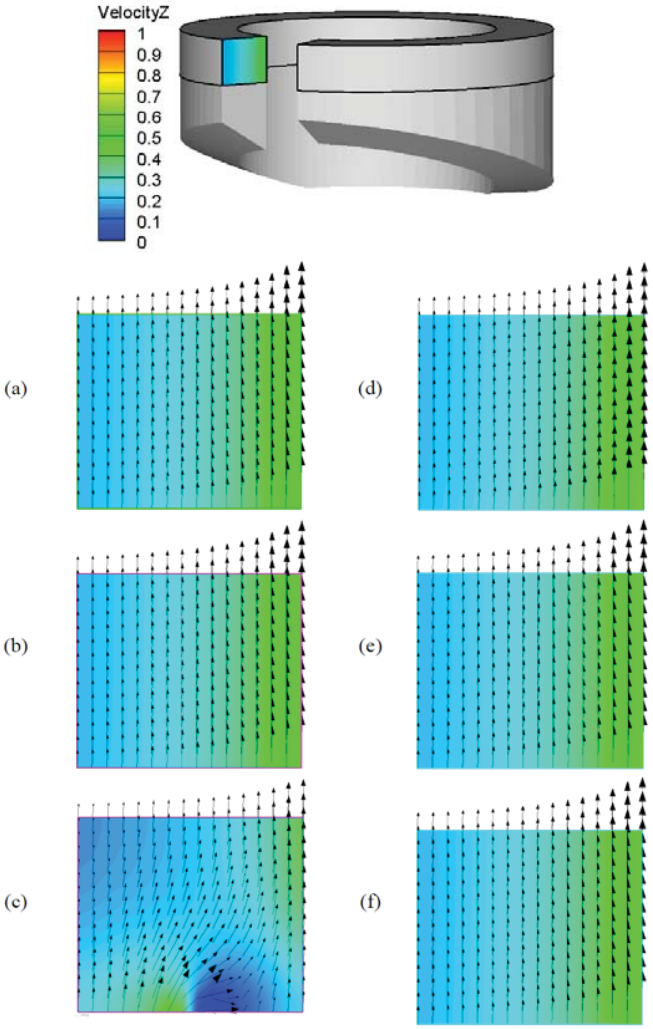

Fig. 14 Models B1–B6, sinter outlet vertical velocity vectors

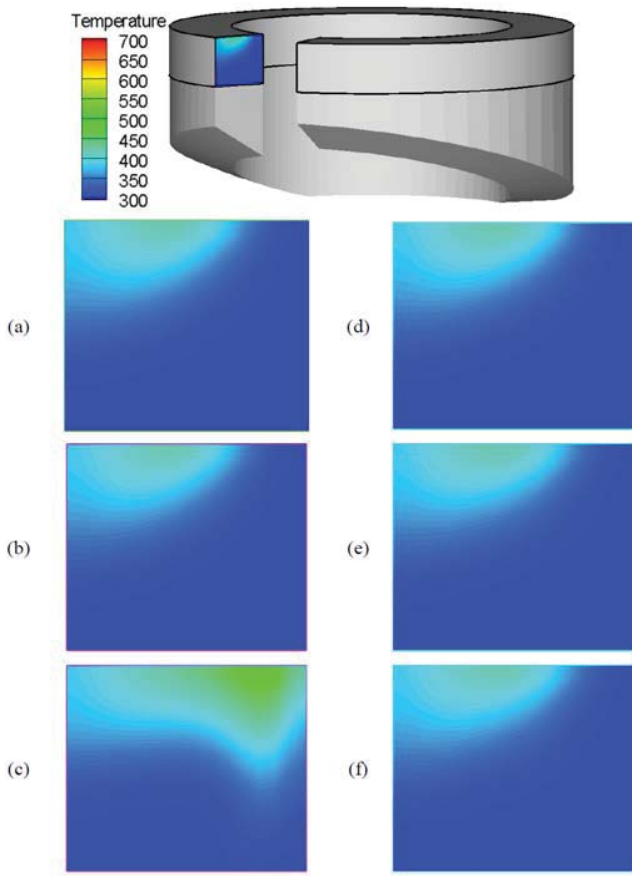

Fig. 15 Models B1–B6, sinter outlet temperature patterns

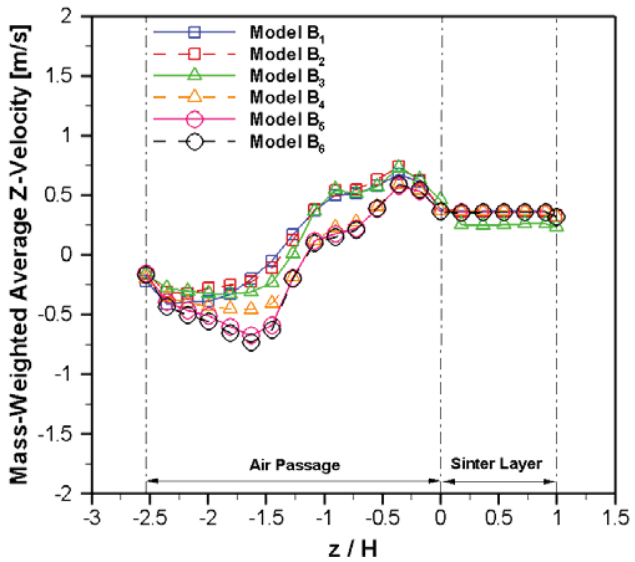

Fig. 16 Models B1–B6, different height cross section vertical direction average velocity relation

D.Effect of Changing the Air Channel Slope Angle on the Thermo Flow Field

From Fig. 17, it could be seen that as the air channel slope increased with the angle, the vertical direction speed within the air channel also gradually increased. However, it was unable to allow the vertical speed flowing across the sinter to have a significant and strong acceleration. Therefore, as shown in Table IX, the mean temperature was 328 K and the slope angle of the air channel was from 0 to 20 degrees, whereas the temperature uniformity was all 0.30. From the cooling index, it could be seen that the changes with the air channel slope angle did not have a significant cooling effect improvement with the sinter outlet temperature.

TABLE IX
INDIVIDUAL CASE OF SLOPE CHANGE -SINTER OUTLET TEMPERATURE COOLING INDEX (CI) AND UNIFORMITY INDEX (UI)

Model	C_1	C_2	C_3	C_4	C_5
Mean temperature (*K*)	328	328	328	328	328
Maximum temperature (*K*)	507	507	507	507	507
Minimum temperature (*K*)	300	300	300	300	300
Temperature difference (*K*)	207	207	207	207	207
CI	0.97	0.97	0.97	0.97	0.97
UI	0.97	0.97	0.97	0.97	0.97

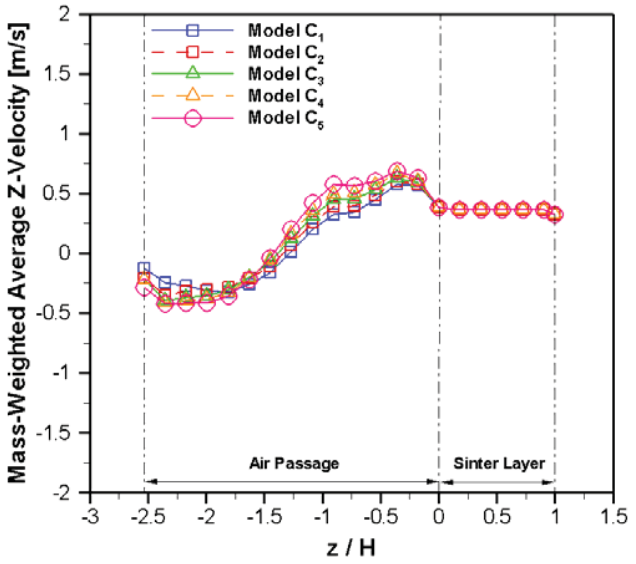

Fig. 17 Models C1–C5, different height cross section vertical direction average velocity relation

TABLE X
CHANNEL GROOVE -SINTER OUTLET TEMPERATURE COOLING INDEX (CI) AND UNIFORMITY INDEX (UI)

Model	D_1	D_2	D_3
Mean temperature (*K*)	328	328	328
Maximum temperature (*K*)	507	507	507
Minimum temperature (*K*)	300	300	300
Temperature difference (*K*)	207	207	207
CI	0.97	0.97	0.97
UI	0.97	0.97	0.97

E. Effect of Changing the Air Channel Slope Exterior on the Thermo Flow Field

From Fig. 18, it can be seen that the surface of the air channel slope is added with a groove design. Model A1 was used as the reference model (named as Model D1) for comparison. The changes with the groove height allocation were unable to make the vertical direction speed to accelerate. Stagnation of the cooling air within the groove caused kinetic energy

consumption with the flow. As seen in Table X, the changes with the groove height were unable to have significant cooling effect improvements with the sinter outlet temperature.

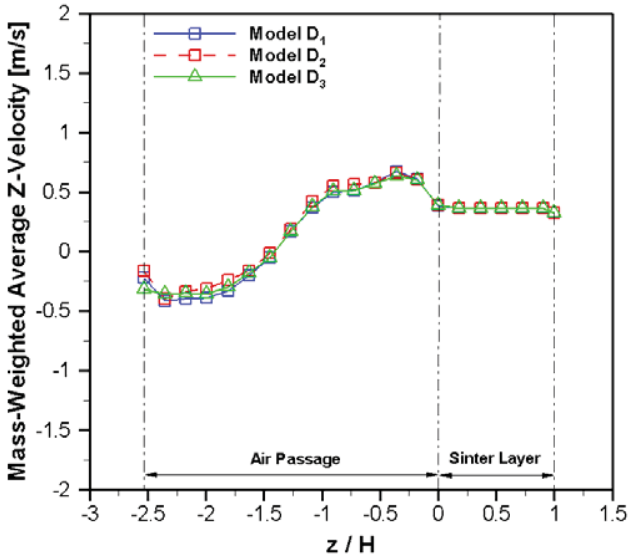

Fig. 18 Models D1–D3, different height cross section vertical direction average velocity relation

TABLE XI
BLOWING FAN INLET TEMPERATURE -SINTER OUTLET TEMPERATURE COOLING INDEX (CI) AND UNIFORMITY INDEX (UI)

Model	E1	E2	E3	E4	E5	E6
Mean temperature (*K*)	328	325	321	318	324	322
Maximum temperature (*K*)	507	506	504	503	504	506
Minimum temperature (*K*)	300	293	285	280	300	281
Temperature difference (*K*)	207	213	219	223	204	225
CI	0.97	0.96	0.95	0.95	0.96	0.96
UI	0.97	1.00	1.03	1.06	0.94	1.06

F. Effect of Changing the Blowing Fan Inlet Temperature on the Thermo Flow Field

The sinter outlet uniformity was discussed when the blowing fan inlet temperature was changed for the typical example. As the cooling air temperature was changed for blowing fans A and B, respectively, the results are shown in Table XI. The sinter outlet mean temperature in Model E2 reduced 1% of Model E1 (typical example), whereas Model E3 reduced 2%, and Model E4 reduced 2.7%. However, the sinter at z/H=1 still existed with high temperatures, which caused poor temperature uniformity when cooler air was blown from a fan. The sinter outlet temperature uniformity in Model E2 raised 3.5% higher than Model E1, whereas Model E3 raised 7.1%, and Model E4 9.7%. In Model E5, the temperatures for blowing fans A and B were 273 K and 300 K, respectively. The sinter outlet mean temperature and temperature uniformity were lowered at the same time. Although the mean temperatures in the other examples were lower than the typical example, the overlarge temperature difference caused the temperature uniformity to be higher than the typical example. It is therefore realized that the temperature cooling index for Model E2 to Model E6 were all better than Model E1 (typical example), obtaining a cooling effect, but only the uniformity index in Model E5 was lower than Model E1 with a reduction of 0.4%.

V. CONCLUSIONS

The study discussed and analyzed the sinter arrangement methods. From the study, the following conclusions were given:

Sinter arrangement method to Model A2 (particle size is greater in the middle of radial direction, and to internal and external sides of decline) of cooling index (CI) and uniformity index (UI) are better than the typical example cooling effect.

Air channel blockage plate set for the installation of sinter outlet temperature does not improve the effect, and Model B3 set the case for the blockage plate cooling effect was the least one.

Changing air channel slope angle, vertical direction as the angle increased speed also rose, but improved temperature of the cooling effect was not a significant upgrade; changing air channel slope exterior of the groove design and unable to increase the vertical direction speed, so that airflow back in the groove to generate flow and consumption kinetic energy, leading to sinter outlet mean temperature higher than the more typical example.

When the blowing fan by the cooling temperature sinter cooler into the lower one, its sinter outlet mean temperature up to significant improve the effect, but the temperature difference also increased, but resulted in poor temperature uniformity.

ACKNOWLEDGMENTS

The author would like to thank Professor S. C. Tzeng of HKUST for providing the related equipment and instruments for the experiments, where the collected experimental data supported this study.

NOTATIONS

A = cross section area, m^2
CI = temperature cooling index, (1)
C = specific heat, $Jkg^{-1}K^{-1}$
E = total energy, J
G = generated terms in turbulent kinetic energy
k_{eff} = effective thermal conductivity, $Wm^{-1}k^{-1}$
k = turbulence kinetic energy, m^2/s^2
κ = permeability, m^2
$\dot{m}$ = mass flow rate, kg/s
p = pressure, Pa
r = radius, m
S = Source term
$\overline{T}$ = numerical simulation of the sinter outlet mean temperature, K
$\overline{T}_{\exp}$ = actual measured data of 31 days for the sinter outlet mean temperature, K
T_i = sinter temperature at each outlet surface, K
UI = uniformity index, (2)
$\vec{u}_r$ = rotational speed, m/s
$\vec{v}_r$ = relative velocity, m/s

ε = turbulent dissipation rate, m^2/s^3
E = porosity
μ = viscosity coefficient, $kg\ ms^{-1}$
ρ = density, kg/m^3
$\vec{\omega}$ = angular velocity, m/s
ϕ = dependent variable

REFERENCES

[1] J. Patrick, R. Barranco, "Carbon Deposits: Formation, Nature, and Characterisation", *COMA/CRF Meeting*, United Kingdom, 2006.
[2] V. Krebs, F. Mareche, G. Furdin, D. Dumay, "Contribution to the Study of Carbon Deposition in Coke Ovens", *Fuel*, Vol. 73, No. 12, 1994, pp. 1904-1910.
[3] Z.J. Hu, K.J. Huttinger, "Mechanisms of Carbon Deposition-a Kinetic Approach", *Carbon*, Vol. 40, No. 4, 2002, pp. 624-628.
[4] K. Norinaga, K.J. Huttinger, "Kinetics of Surface Reactions in Carbon Deposition from Light Hydrocarbons", *Carbon*, Vol. 41, No. 8, 2003, pp. 1509-1514.
[5] Y. Z. Fang, P. Huang, Z. Zhang, Y.P. Cao, M.L. Jin, "Analysis on the Growth Mechanism of Carbon Deposits in Coke Oven", *Clean Coal Technology*, Vol. 17, No. 5, 2011, pp. 36-39. (In Chinese)
[6] Z. Z. Wang, Z. F. Zhan, W. D. Wang, W. D. Zhang, X. Q. Zhang, H. S. Wang, "Analysis and Research on Coal Moisture Control Technology", *Applied Energy Technology*, No. 3, 2014, pp. 5-9. (In Chinese)
[7] A. Furusawa, T. Nakagawa, Y. Maeno, I. Komaki, "Influence of Coal Moisture Control on Carbon Deposition in the Coke Oven Chamber", *ISIJ*, Vol. 38, No. 12, 1998, pp. 1320-1325.
[8] V. Krebs, G. Furdin, J.F. Mareche, D. Dumay, "Effects of Coal Moisture Content on Carbon Deposition in Coke Ovens", *Fuel*, Vol. 75, No. 8, 1996, pp. 979-986.
[9] T. Nakagawa, T. Kudo, Y. Kamada, T. Suzuki, Y.Suzuki, I. Komaki, "Control of Carbon Deposition in the Free Space of Coke Oven Chamber by Injecting Atomized Water", *ISIJ*, Vol. 68, No. 7, 2002, pp. 386-392.
[10] V. Zymla, F. Honnart, "Coke Oven Carbon Deposits Growth and Their Burning Off", *ISIJ*, Vol. 47, No. 10, 2007, pp. 1422-1431.
[11] C. Z. Lu, Y. P. Cao, "Study on Properties of Carbon Deposite in Coking Chamber and its Reaction Kinetics with Air", *Fuel & Chemical Processes*, Vol. 41, No. 1, 2010, pp. 15-18.
[12] S. R. Turns, *An Introduction of Combustion Concepts and Applications*, 3rd Ed., McGraw Hill, 2012.
[13] H. S. Caram, N. R. Amundson, "Diffusion and Reaction in a Stagnant Boundary Layer about a Carbon Particle", *Ind. Eng. Chem., Fundam.*, Vol. 16, No. 2, 1977, pp. 171-181.
[14] G. Adomeit, W. Hocks, K. Henriksen, "Combustion of a Carbon Surface in a Stagnation Point Flow Field", *Combustion and Flame*, Vol. 59, 1985, pp. 273-288.
[15] F. Yi, J. Fan, D. Ki, S. Lu, K. Luo, "Three-dimensional Time-dependent Numerical Simulation of a Quiescent Carbon Combustion in Air", *Fuel*, Vol. 90, 2012, pp. 1522-1528.
[16] P. A. Nikrityuk, M. Grabner, P. Kestel, B. Meyer, "Numerical Study of the Influence of Heterogeneous Kinetics on the Carbon Consumption by Oxidation of a Single Coal Particle", *Fuel*, Vol. 114, 2013, pp. 88-98.
[17] L. X. Zhou., *Combustion Theory and Chemical Fluid Dynamics*, Science Press, Moscos, 1986.
[18] B. F. Magnussen, B. H Hjertager, "On Mathematical Modeling of Turbulent Combustion with Special Emphasis on Soot Formation and Combustion" *Symposium (Int.) on Combustion*, Vol. 16, 1977, pp. 719-729.
[19] T. H. Shih, W. W. Liou, A. Shabbir, Z. Yang, J. Zhu, "A New k-ε Eddy-viscosity Model for High reynolds Number Turbulent Flows – Model Development and Validation," *Computer Fluids*, vol. 23, 2012, pp. 227-238.
[20] K. K. Kuo, *Principle of combustion*. New York: John Wiley and Sons, 1986.
[21] P. Cheng, "Two-dimensional radiating gas flow by a moment method," *AIAA Journal*, vol. 2, 1964, pp. 1662-1664.
[22] T. F. Smith, Z. F. Shen, and J. N. Friedman, "Evaluation of coefficients for the weighted sum of gray gases model," *J. Heat Transfer*, vol. 104, 1982, pp. 602-608.
[23] P. Forchheimer, "Water Movement through Soil," Time Ver. German Ing. Vol. 45, 1901, pp. 1782-1788.
[24] M. Kaviany, "Principle of Heat Transfer in Porous Media," Second Edition, Springer-Verlag New York, 1995
[25] Kline SJ, Mcclintock FA (1953). Describing Uncertainties in Single-Sample Experiments. Mechanical Engineering 75:3-8.
[26] R.J. Moffat, "Contributions to the Theory of Single-sample Uncertainty Analysis," ASME Journal of Fluid Engineering, Vol. 104, 1986, pp. 250-260.